

Improving Estimation of Parameters in Photovoltaic Models Using Two-Level Layered Physics-Informed Neural Networks

Nikta Shamsmohammadi , Member, IEEE, Giovanni Spagnuolo , Fellow, IEEE, José del Campo-Ávila , Esteban José Palomo , and Llanos Mora-López 

Abstract—Accurate estimation of parameters in photovoltaic models is essential to improve system monitoring, control, and diagnostics. In this study, a novel two-level layered physics-informed neural network (PINN) architecture is proposed to estimate the parameters irradiance (G) and temperature (T), and junction capacitance (C_{j0}) in a dynamic single-diode PV model. In case no noise affects the PV current and voltage waveforms, the proposed method achieves errors equal to 0.25% for G , 1.5% for T , and 2.1% for C_{j0} . Compared to traditional optimization methods, the two-level layered PINN shows a better performance, particularly in learning the nonlinear behavior of C_{j0} . Sensitivity analysis under additive Gaussian noise (0% –5%) confirms the robustness of the approach, with a slight increase of the identification error. The results confirm the effectiveness of incorporating physical knowledge into neural networks for robust and reliable parameter estimation in dynamic photovoltaic systems.

Index Terms—Parameter identification, photovoltaic (PV) dynamic model, two-level layered physics-informed neural network (PINN).

I. INTRODUCTION

PARAMETER estimation in photovoltaic (PV) modules is fundamental for control applications and supports various model-based monitoring, fault detection, and diagnostics aimed at improving system performance and reliability. In PV semiconductors, the depletion capacitance (C) arises from the separation of free charge carriers within the p-n junction, forming a space-charge region. According to [1], this capacitance directly depends on the instantaneous voltage and current applied to the

modules, as these variables dynamically alter the width of the depletion region. Under transient conditions, the redistribution of charge carriers and the evolution of the internal electric field over time lead to a dynamic and nonlinear behavior of C . By analyzing the transient behavior of C , we can perform diagnostics and extract dynamic information about the operational state of the PV modules [2]. This phenomenon is relevant in crystalline silicon (c-Si) PV cells, where the depletion capacitance plays a central role in determining the device's dynamic response. In such cells, the junction capacitance exhibits a nonlinear dependence on both voltage and current, due to the modulation of the depletion region width. The inherent characteristics of c-Si technology make it a suitable option for time-domain modeling under transient conditions. Although previous studies have investigated this behavior using frequency-domain methods such as impedance spectroscopy [1], [3], these techniques often involve complex analysis. In contrast, this study uses a time-domain approach, which provides a simpler and effective way to capture the dynamic capacitance behavior of silicon-based PV modules [11].

Different models are used in the literature to describe PV modules. The single-diode model (SDM) is one of the most commonly used. Various methods are used for system analysis and parameter estimation. According to the literature [4], [5], [6] data-driven methods are widely used for parameter estimation; however, these approaches neglect the physical laws of the system, potentially leading to inaccurate or nonphysical results. Physics-based methods rely on governing equations but usually struggle with complex nonlinear systems. Recently, a new approach called physics-informed neural networks (PINNs) was introduced [7]. This method incorporates physical laws into the loss function of the neural network. As a result, the model learns from both data and physics, which enables PINNs to perform well even when the available data are noisy or limited [8]. Unlike traditional supervised learning methods, PINNs do not rely on large labeled datasets. The integration of advanced neural network architectures with the framework of PINNs has led to the development of models with enhanced capabilities for solving complex scientific problems. Although recent developments have significantly improved the capabilities of PINNs, the issue of weak convergence with respect to certain physical parameters remains a challenge. This challenge is largely due

Received 28 May 2025; revised 17 July 2025; accepted 17 August 2025. Date of publication 17 September 2025; date of current version 23 October 2025. This work was supported in part by the PRIN2022PNRR “ISOPVDT – An isomorphism-based digital twin for mismatched photovoltaic arrays control and diagnosis” (funded by the European Union – Next Generation EU, Mission 4 Component 1,) under Grant CUP D53D23016000001, and in part by the Dottorato di Interesse Nazionale “Photovoltaics.” (Corresponding author: Nikta Shamsmohammadi.)

Nikta Shamsmohammadi and Giovanni Spagnuolo are with the Dipartimento di Ingegneria dell'Informazione ed Ingegneria Elettrica e Matematica Applicata (DIEM), Università degli Studi di Salerno, 84084 Fisciano (SA), Italy (e-mail: nshamsmohammadi@unisa.it).

José del Campo-Ávila, Esteban José Palomo, and Llanos Mora-López are with the Departamento de Lenguajes y Ciencias de la Computación, Universidad de Málaga, 29071 Málaga, Spain (e-mail: llanos@uma.es).

Digital Object Identifier 10.1109/JPHOTOV.2025.3604854

to the nonlinear influence of such parameters in the governing equations.

In this work, we aim to improve the use of PINN framework by taking into account the nonlinear nature of the capacitor to achieve more accurate parameter estimation. The main contributions of this study are summarized as follows:

- 1) Developing neural networks with more advanced architectures to enhance the accuracy of estimating nonlinear parameters exhibiting complex behavior;
- 2) Time-domain analysis without requiring conversion to the frequency domain;
- 3) Robustness and reliable parameter estimation despite the presence of noise.

The rest of the article is organized as follows. Section II presents a brief overview of the literature about PINN. Section III outlines nonlinear dynamic SDM of photovoltaic modules. Section IV presents PV panel characteristics and parameter modeling. Dataset used for proposed model is presented in Section V. Section VI describes neural network design for two-level layered PINN. Section VII presents corresponding results. Section VIII outlines improvements and future outlook. Finally, Section IX concludes this article.

II. RECENT APPROACHES IN PINN-BASED POWER SYSTEMS PARAMETERIC IDENTIFICATION

In recent years, PINNs emerge as a powerful and innovative approach for modeling, analysis, and control of power systems and power electronics. By integrating physical knowledge of the system with the capabilities of machine learning, PINNs offer an effective solution to challenges such as data scarcity, nonlinear behavior, and complex system dynamics [18].

For instance, PINNs serve effectively in tasks such as state and parameter estimation, where accurate modeling remains crucial despite limited or noisy measurements [8]. For example, in [19], a PINN-based approach enables simultaneous estimation of dynamic states and system parameters in power generators using limited PMU data. The method incorporates differential equations as physical constraints during training. Its strengths include robustness to noisy data and the ability to estimate multiple variables concurrently. However, it relies on accurate physical models, requires careful hyperparameter tuning, and involves high computational costs for complex systems. Also, Wang and Yu, [20] presented a novel physics-informed graph neural network methodology that enables accurate state estimation in power systems. Key strengths include robustness to noise, reduced dependency on labeled data, and strong generalization capability. However, the method relies on accurate network topology, involves complex implementation, and lacks wide validation on real-world power systems.

One of the main challenges in parameter estimation of power electronic converters is the limited availability of measurement data and the need for accurate modeling. In [16], a novel method estimates the parameters of a buck converter using physics-informed machine learning. By leveraging PINNs and peak-to-peak voltage and current data, this approach achieves high estimation accuracy without requiring disturbance

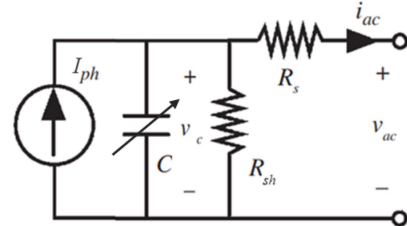


Fig. 1. Dynamic and nonlinear SDM of the PV module.

injection. However, a notable weakness remains the lack of a systematic approach to determine the optimal weighting between the physical model and data terms in the loss function.

To address these limitations, particularly the slow convergence of PINNs in parameter estimation tasks and the long training times, this article proposes a new network architecture specifically designed for PV systems. By using a dedicated two-level layered PINN, the proposed approach significantly improves convergence speed and scalability. Furthermore, to overcome the challenge of manually tuning the weighting coefficient λ between the data loss and physics-based loss in the objective function, the method employs an adaptive strategy where λ changes dynamically during training. This leads to a more balanced optimization process and enhances the robustness and accuracy of parameter estimation under noisy or limited data conditions.

The following sections detail the formulation of the PV system model and the integration of physical laws into the network training. Specifically, the mathematical modeling of the system, the design of the loss function, and the implementation of the proposed two-level layered PINN form a comprehensive framework that enables accurate and efficient parameter estimation while preserving physical consistency throughout the learning process.

III. DYNAMIC PV SDM

Fig. 1 illustrates the SDM of the PV module, in which the diode is replaced by a nonlinear capacitance that varies with both current and voltage [1], [2].

The following expression defines the capacitance model as a function of both voltage and current:

$$C(V_{ac}(t), i_{ac}(t)) = \frac{C_{j0}}{\sqrt{1 + \frac{(V_{ac}(t) + R_s i_{ac}(t))}{V_j}}} \quad (1)$$

where C_{j0} represents the junction capacitance, while V_j refers to the built-in junction. These parameters define how the depletion capacitance changes with voltage in the circuit model. The current through the capacitor is obtained by differentiating the charge with respect to time.

Assuming $Q(t) = C(v_c(t)) \cdot v_c(t)$, the expression for charge is as follows:

$$Q(t) = \frac{C_{j0} V_{ac}(t)}{\sqrt{1 + \frac{(V_{ac}(t) + R_s i_{ac}(t))}{V_j}}} \quad (2)$$

The capacitive current can be expressed as the time derivative of the charge as follows:

$$i_c(t) = \frac{dQ(t)}{dt} = \frac{d}{dt} \left(\frac{C_{j0} V_{ac}(t)}{\sqrt{1 + \frac{(V_{ac}(t) + R_s i_{ac}(t))}{V_j}}} \right). \quad (3)$$

The capacitive current can also be written as follows:

$$i_c(t) = C_{j0} \frac{d}{dt} \left(\frac{V_{ac}(t)}{\sqrt{1 + \frac{(V_{ac}(t) + 2R_s i_{ac}(t))}{V_j}}} \right). \quad (4)$$

According to Kirchhoff's current law, the photogenerated current I_{ph} is divided among the capacitive current $i_c(t)$, the current through the shunt resistor $i_{R_{sh}}(t)$, and the output current $i_{ac}(t)$, leading to the following relation:

$$I_{ph} - i_c(t) - i_{R_{sh}}(t) - i_{ac}(t) = 0. \quad (5)$$

The current flowing through the shunt resistance is as follows:

$$i_{R_{sh}}(t) = \frac{v_c(t)}{R_{sh}} \quad (6)$$

So we have

$$i_{ac}(t) = I_{ph} - C_{j0} \frac{d}{dt} \left(\frac{V_{ac}(t)}{\sqrt{1 + \frac{(V_{ac}(t) + 2R_s i_{ac}(t))}{V_j}}} \right) - \frac{v_c(t)}{R_{sh}}. \quad (7)$$

And the voltage-current relationship is as follows:

$$v_c(t) = V_{ac}(t) - R_s i_{ac}(t). \quad (8)$$

Using this relation in the total current equation gives the following:

$$\begin{aligned} \frac{(v_c(t) - V_{ac}(t))}{R_s} &= I_{ph} \\ &- C_{j0} \frac{d}{dt} \left(\frac{V_{ac}(t)}{\sqrt{1 + \frac{(V_{ac}(t) + 2R_s i_{ac}(t))}{V_j}}} \right) - \frac{v_c(t)}{R_{sh}}. \end{aligned} \quad (9)$$

The final equation is as follows:

$$\begin{aligned} \frac{d}{dt} \left(\frac{V_{ac}(t)}{\sqrt{1 + \frac{(V_{ac}(t) + 2R_s i_{ac}(t))}{V_j}}} \right) &= \frac{1}{C_{j0}} \left(I_{ph} \right. \\ &\left. + \frac{V_{ac}(t)}{R_{sh}} - v_c(t) \left(\frac{1}{R_{sh}} + \frac{1}{R_s} \right) \right). \end{aligned} \quad (10)$$

Equation (10) describes the nonlinear variations of the junction capacitance with respect to the input voltage and current.

This equation is used in the following section to model the dynamic behavior of the PV module.

IV. PV PANEL CHARACTERISTICS AND PARAMETER MODELING

Table I presents the electrical characteristics of the Kyocera KC175GHT-2 panel under standard test conditions (STCs), as provided in the manufacturer's datasheet, along with the values of the static parameters identified in [9].

TABLE I
KYOCERA KC175GHT-2 DATASHEET VALUES AT STC AND SDM IDENTIFIED VALUES FROM [9]

Characteristics at STC		SDM Parameters	
V_{oc}	29.2 [V]	I_{ph}	8.09 [A]
I_{sc}	8.09 [A]	I_s	2.0722 [nA]
MPP coordinates	23.6 [V], 7.42 [A]	η	1.0730
Thermal Coefficients	$\alpha_v = -109$ [mV/ $^{\circ}$ C] $\alpha_I = 3.18$ [mA/ $^{\circ}$ C]	R_s	0.2185 [Ω]
Number of cells	48	R_{sh}	93.0571 [Ω]

According to the literature [10], several essential parameters of SDM depend on irradiance (G) and temperature (T). The equations are as follows:

$$I_{ph}(G, T) = \frac{G}{G_{STC}} [I_{ph,STC} + \alpha(T - T_{STC})] \quad (11)$$

$$R_s(G, T) = R_{s,STC} \quad (12)$$

$$R_{sh}(G, T) = R_{sh,STC} \cdot \frac{G_{STC}}{G}. \quad (13)$$

We considered the value for $R_{s,STC}$, $R_{sh,STC}$, and $I_{ph,STC}$ based on Table I. G_{STC} and T_{STC} are the irradiance and temperature under STC condition ($G_{STC} = 1000$ W/m², $T_{STC} = 25^{\circ}$ C). α is the temperature coefficient of the current and $\alpha = 3.18$ mA/ $^{\circ}$ C based on Table I.

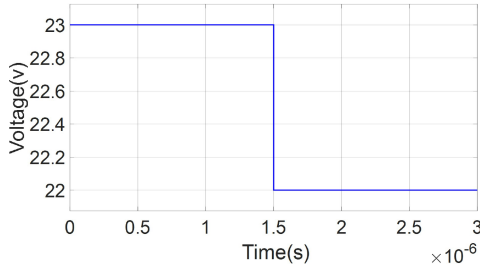
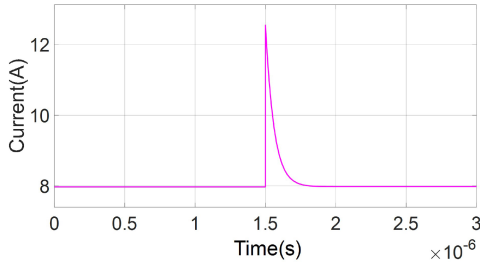
From (11)–(13), it can be observed that the SDM parameters are functions of G and T . Therefore, estimating G and T using the step waveform and step response waveform is sufficient to determine the dependent parameters, eliminating the need to estimate them separately.

On the other hand, C_{j0} in (10) represents the junction capacitance. Its explicit dependence on irradiance G and temperature T is not established in the literature. In this study, C_{j0} is considered as an independent dynamic component and is estimated separately.

In the next section, we describe the structure of the dataset, the parameter settings, and the noise injection process used for training and evaluating the proposed model.

V. DATASET

The dataset in this study is synthetically generated using a dynamic simulation of the equivalent PV circuit model implemented in Simulink. The input voltage $v_{in}(t)$ reflects typical maximum power point tracking (MPPT) [12] behavior, and the PV output current $i_{ac}(t)$ represents the corresponding SDM response. Initially, noise is not added to the Simulink simulation to allow accurate analysis of the performance of the proposed two-level layered PINN identification method under different controlled conditions. The PV voltage and current datasets serve as input to the PINN to estimate the target parameters under both noisy and noise-free conditions in Python. To evaluate the robustness of the proposed PINN model, Gaussian noise with standard deviations ranging from 0% to 5% is added to the PV current waveform. Each noise level scenario repeats ten

Fig. 2. $v_{ac}(t)$ in Simulink MATLAB.Fig. 3. $i_{ac}(t)$ in Simulink MATLAB.

times with different random seeds to ensure statistical reliability. By simulating these inputs under varying noise conditions, the model's parameter estimation process shows its sensitivity and stability systematically. All simulations take place under STC, with irradiance at 1000 W/m^2 and temperature at 25°C .

As shown in Fig. 2, a stepwise voltage is applied to SDM, which is typical of MPP tracking scenarios. The resulting current response, representing the system's behavior under MPP perturbation, is illustrated in Fig. 3.

The following sections present the design of the two-level layered PINN, demonstrating accurate parameter estimation while complying with the physical constraints of the model.

VI. NEURAL NETWORK DESIGN FOR TWO-LEVEL LAYERED PINN

PINNs can be used for both direct and inverse problems [13]. In direct problems, they solve differential equations by learning solutions that follow physical laws. In inverse problems, they estimate unknown parameters from observed data. In both cases, the main advantage of PINNs is that they include physics directly in the training process through the loss function. While the data-driven part is modeled by a feedforward neural network, the physics-based part ensures that the solution stays consistent with the governing equations [14].

A dynamic system is considered as presented in [7], which governing partial differential equation (PDE) are given below:

$$u_t + \mathcal{N}[u; \lambda] = 0, \quad x \in \Omega, t \in [0, T] \quad (14)$$

$$f := u_t + \mathcal{N}[u; \lambda] \quad (15)$$

$u(t, x)$ is the unknown solution, implicitly defined through its time derivative u_t and the nonlinear operator $\mathcal{N}[u; \lambda]$, which together govern its evolution over space and time. The goal is

to find $u(t, x)$ such that the PDE is satisfied within the spatial domain Ω and over the time interval $[0, T]$, subject to initial and boundary conditions. In other words, $u(t, x)$ is the target solution to be learned, while f is the residual that measures how well $u(t, x)$ satisfies the governing PDE [16].

As illustrated in Fig. 2, the input voltage suddenly drops from 23 V to 22 V at approximately 1.5×10^{-6} s. This sudden change causes a transient response in the output current (see Fig. 3).

The following sections provide detailed explanations of the network architecture and the loss function design.

A. Loss Function Formulation

This section outlines the formulation of the loss function, which combines data consistency with physical constraints by incorporating the governing differential equations into the training process.

In PINNs, the loss function integrates both physical laws and observational data to guide the learning process. It consists of a physics-based term that enforces the governing differential equations, alongside a data-driven term that ensures agreement with measured values. The relative influence of each term is adjusted using weighting factors, enabling the network to achieve accurate predictions while remaining consistent with the underlying physics. Based on our study, the loss function is formulated as follows:

$$\begin{aligned} \mathcal{L}(t, \theta) = & \frac{1}{M} \sum_{i=1}^M \left(\left[\frac{dV_c}{dt} - u_{\text{PINN}}(t_i; \theta) \right]^2 \right) \\ & + \lambda_1 \cdot \frac{1}{M} \sum_{j=1}^M (u_{\text{PINN}}(t_j; \theta) - u_{\text{obs}}(t_j))^2 \\ & + \lambda_2 \cdot \frac{1}{M} \sum_{k=1}^M ([I_{\text{ph,STC}} + \alpha(T - T_{\text{STC}})] \cdot u_{\text{PINN}}(t_k; \theta)) \end{aligned} \quad (16)$$

The loss function in (16) is composed of three main terms, each reflecting a different aspect of the learning objective. The first term represents the physics-based component, which penalizes the discrepancy between the predicted value $u_{\text{PINN}}(t; \theta)$ and the time derivative of the capacitor voltage $\frac{dV_c}{dt}$. This term ensures that the neural network's output adheres to the governing differential equation, thus embedding physical consistency into the training process.

The second term, corresponds to the data-driven loss, which minimizes the error between the model's predictions and the observed measurements $u_{\text{obs}}(t)$. This term helps guide the learning process using available data and becomes especially important in estimating parameters with highly nonlinear behavior, such as C_{j0} . The coefficient λ_1 controls the contribution of the data-driven term.

The third term, introduces temperature dependence into the loss formulation. Including this term helps the network attribute temperature-induced variations to the correct physical sources,

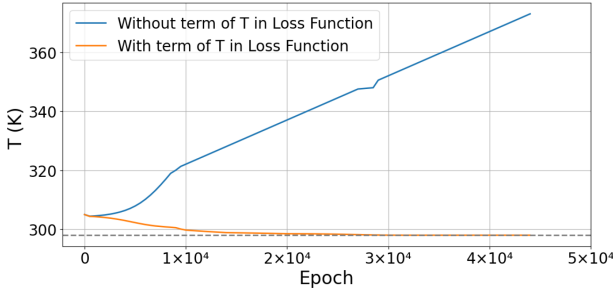


Fig. 4. Effect of including the temperature term in the loss function. The model without the T term in loss function (blue curve) becomes unstable, while the model with the T term in loss function (orange curve) converges smoothly.

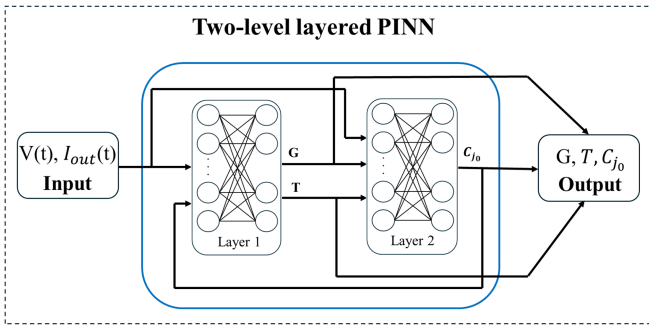


Fig. 5. Architecture of the proposed two-level layered PINN. The Layer 1 focuses on estimating the G and T . These estimates are then used by the Layer 2 to refine the model output and estimate the junction C_{j0} .

improving estimation accuracy and preventing parameter cross-dependency [15]. To ensure its impact is properly captured, it is weighted by λ_2 .

As shown in Fig. 4, without including T in the loss function, the model misattributes temperature effect to other parameters, resulting in biased estimates.

According to (16) in our loss function framework, $M = 150$ represents the number of training samples used for the data loss. The loss weighting factors are empirically set to $\lambda_1 = 1000$ for the data loss, ensuring that the model closely fits the observed data, and $\lambda_2 = 10$ to maintain the temperature effect's influence without letting it dominate the training process. We have searched for the best value for λ_1 and λ_2 in the range $[1, 1500]$ using 100 steps.

B. Network Architecture

This section describes the structure of the proposed two-level layered PINN, including the number of layers, activation functions, and parameter assignments used in each stage of the model.

For input data, only the transient part of the current is used, and the dataset consists of 150 samples containing voltage and current values over time. Using only the transient region helps reduce the amount of data and improves the efficiency of training as well as the accuracy of parameter estimation. The structure shown in Fig. 5 represents a two-level layered PINN developed for parameter estimation in PV systems. This model combines

TABLE II
NETWORK ARCHITECTURE DESIGNED BASED ON THE BEHAVIORAL DIFFERENCES OF PARAMETER C_{j0}

Network Information	Network for C_{j0}	Network for T, G
Number of Layers	28	30
Neurons per Layer	3	3
Activation Function	Tanh	Tanh
Optimizer	AdamW	AdamW
Learning Rate	2×10^{-4}	5×10^{-4}
L2 Regularizer	1×10^{-8}	1×10^{-8}
Epochs	50001	50001
Batch Normalization	Yes	No
Residual Connections	Yes	No
Layer Normalization	Yes	No

measurement data with physical laws described by differential equations.

The architecture includes two connected neural subnetworks. The parameters I_{ph} , R_s , and R_{sh} themselves depend on environmental conditions such as irradiance G and temperature T . The parameter C_{j0} is treated separately from R_s , R_{sh} , and I_{ph} because the model does not express it as a function of temperature or irradiance, but only as dependent on voltage and current. These dependencies are implicitly encoded in the first layer of the proposed two-level layered PINN (see Fig. 5), which receives voltage and current over time and learns to estimate G and T . This layer starts by minimizing the loss associated with environmental variables and system-level behavior, where the loss function is constructed based on the governing differential equation (10). As the training progresses and the error in estimating G and T decreases, the network gradually enables the second layer to refine the output dynamics by focusing on the internal parameter C_{j0} , which appears explicitly in the differential structure of (10). Once the external conditions are sufficiently captured and the system behavior stabilizes, the second layer effectively starts to learn C_{j0} with higher accuracy. This staged training process prevents interference between parameter spaces and allows the model to better capture the nonlinear transient behavior of the PV system. The layered strategy ensures that learning follows the structure of the physical model, improving both robustness and accuracy.

Table II summarizes the architectures of the two-level layered PINN used to estimate the parameters. C_{j0} has a more complex and nonlinear behavior. Batch normalization, residual connections, and layer normalization are used to improve learning and estimation accuracy for C_{j0} . Batch normalization stabilizes training by reducing internal covariate shift, while residual connections improve gradient flow. Layer normalization is also applied to enhance robustness, particularly in deeper layers. The use of a two-level layered PINN architecture improves the overall estimation performance by decoupling the learning of global and local parameters. Estimating irradiance and temperature in the first stage allows the second stage to operate on more physically informed inputs, resulting in faster convergence, reduced

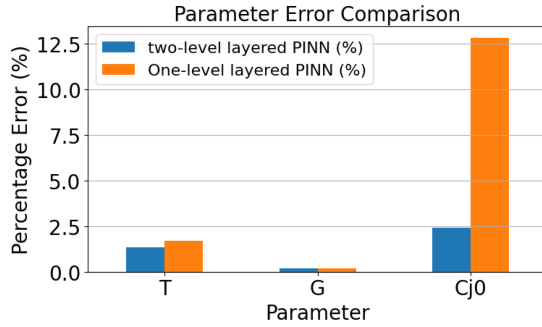


Fig. 6. Comparison of parameter estimation errors between the one-level layered PINN and the two-level layered PINN approach. The results show that while both methods achieve low errors for parameters T and G , the two-level layered PINN significantly reduces the estimation error for C_{j0} , indicating its superior ability to capture complex parameter dynamics.

TABLE III
VALUE RANGES USED FOR EACH PARAMETER DURING TRAINING

Parameter	Range
G	[700 W/m ² , 1500 W/m ²]
T	[270 K, 320 K]
C_{j0}	[0.1×10^{-7} F, 3.5×10^{-7} F]

training complexity, and improved accuracy in estimating C_{j0} that changes with voltage and current.

Fig. 6 illustrates the impact of using a one-level layered PINN versus a two-level layered PINN architecture, where the percentage error of each parameter is compared to evaluate the performance of both models.

In the following, we present the implementation of the proposed network and discuss the results of its training and parameter estimation performance.

VII. NETWORK TRAINING RESULTS

Although PINNs do not require set initial values or parameter bounds, we applied physically meaningful limits to improve training stability and avoid nonphysical results. We also used bounds to avoid unnecessary search, as shorter training time is preferred. Table III summarizes the value ranges used in the training process. The initial values for all parameters are randomly assigned, and the model is trained using 150 data points taken from the transient region of the current response.

The output current is illustrated in Fig. 7, demonstrating that the response predicted by the PINN closely matches the true output throughout the transient region.

Fig. 8 presents the convergence behavior of the estimated parameters T , G , and C_{j0} over the training epochs. As illustrated, all parameters gradually converge to their true values over time, which are considered reference values under STC. The values of T and G are defined under STC as $T = 298^\circ\text{K}$ and $G = 1000 \text{ W/m}^2$, and the value of C_{j0} is taken to be $1.6 \times 10^{-7} \text{ F}$. This consistency supports the assumption that the network effectively identifies the underlying physical parameters governing the system dynamics during training.

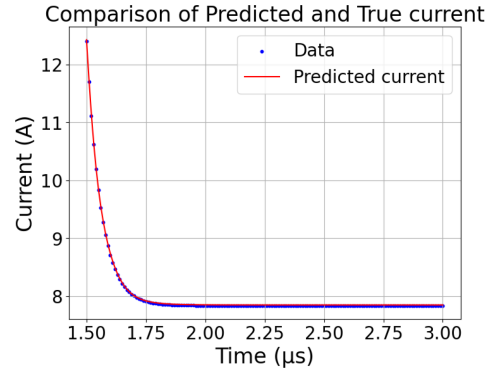


Fig. 7. Comparison of simulated $i_{ac}(t)$ and PINN-identified waveform.

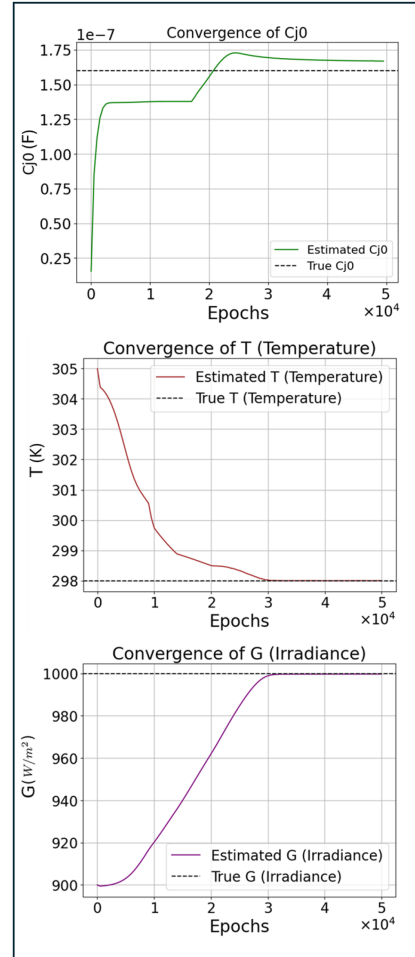


Fig. 8. Evolution of parameters during training: G , T , and C_{j0} .

To evaluate the performance of different estimation methods, the percentage errors for each parameter are presented in Fig. 9. The genetic algorithm (GA) [5] and particle swarm optimization (PSO) [6] are data-driven approaches that rely on input data, without incorporating physical knowledge of the system. To ensure a fair comparison with the proposed PINN model, both GA and PSO were implemented with consistent tuned configurations. According to the literature [6], we employ more

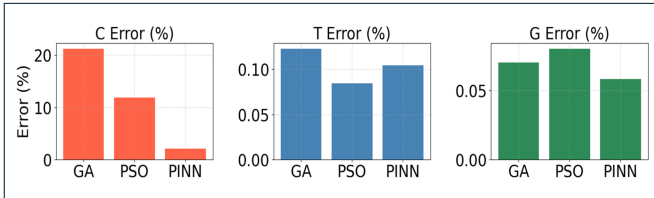


Fig. 9. Comparison of percentage errors in estimating the parameters C_{j0} , G , and T using GA, PSO, and PINN. While all three methods show similar and low errors for G and T , the PINN significantly outperforms the data-driven approaches (GA and PSO) in estimating C_{j0} , demonstrating its advantage in capturing more complex system behaviors.

robust hyperparameters to improve the accuracy of parameter estimation using GA and PSO.

For the GA, we use a population size of 50 and run the optimization over 50 000 generations. Parent solutions combine using arithmetic crossover, and mutations are introduced with a 5% probability by applying small perturbations to the C_{j0} , T , and G values.

For the PSO, we use a swarm size of 50 and conduct the optimization over 50 000 generations within the same search space. The inertia weight is set to 0.7, and both the cognitive and social acceleration coefficients are fixed at 1.5 to balance exploration and exploitation.

Both methods use the parameter boundaries defined in Table III, and these values are determined through empirical testing.

In contrast, the PINN integrates both input data and the underlying physical laws governing the system, leading to more informed and potentially more accurate estimations. All the methods demonstrate strong performance in estimating the (T) and (G), with comparable and minimal percentage errors. However, a significant discrepancy arises in the estimation of C_{j0} . The two previous methods, exhibit noticeably higher errors, suggesting that relying solely on observed data insufficient for accurately capturing the complex behavior of C_{j0} .

To examine how noise influences the parameter identification process, according to [8], Gaussian noise with levels from 0% to 5% is added to the $i_{ac}(t)$ samples. Fig. 10 shows how increasing noise levels affect the accuracy of the estimated output current, with RMSE increasing consistently from 0% to 5%.

Fig. 11 presents the percentage error distributions for the estimated parameters C_{j0} , G , and T under different levels of Gaussian noise (0% to 5%) added to the $i_{ac}(t)$. For each noise level, the experiment was repeated 10 times to ensure statistical reliability, and the results reflect the variability and robustness of the estimation process under noisy conditions.

The estimation error of C_{j0} for 10 times increases from approximately 2.1% at 0% noise to around 5.3% at 5% noise, with noticeable growth in variance and outliers beyond 3% noise. For parameter G , the error remains consistently low, increasing slightly from 0.23% to 0.29% across all noise levels. Similarly, the median error of T changes from about 1.4% at 0% noise to 1.7% at 5%, showing only a marginal increase. These results indicate that C_{j0} is significantly more affected by noise

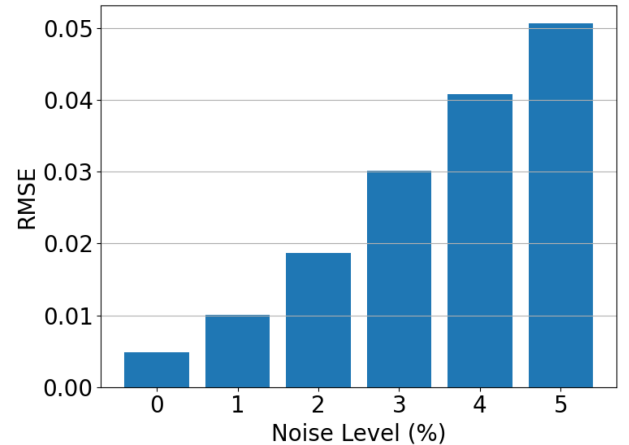


Fig. 10. RMSE values for different noise levels affect the accuracy of the estimated output current.

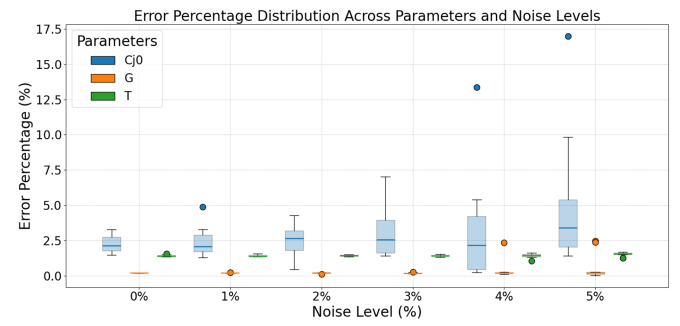


Fig. 11. Distribution of error percentages in estimating parameters C_{j0} , G , and T across different Gaussian noise levels (0% to 5%) applied to $i_{ac}(t)$. As the noise level increases, the estimation error for C_{j0} shows greater variation and sensitivity compared to G and T , which remain relatively stable and less affected.

compared to G and T . These box plots effectively capture both the central tendency (median error) and the spread (variance and presence of outliers) of the estimation accuracy under noisy conditions. A wider interquartile range and larger number of outliers, especially in the case of C_{j0} , indicate greater sensitivity and higher estimation uncertainty due to noise. This heightened sensitivity of C_{j0} to noise can be attributed to its physical role in the system. As a junction capacitance, C_{j0} primarily governs the transient response of the circuit during high-frequency or switching conditions. In such transition regions, small fluctuations in the current or voltage can lead to disproportionately large variations in the estimated capacitance due to its nonlinear dependence on voltage. Unlike parameters such as G or T , which influence the steady-state characteristics more directly and are inferred from longer term signal behavior, C_{j0} is inherently linked to fast, high-frequency dynamics where noise has a more immediate and amplified effect.

VIII. ESTIMATION IMPROVEMENTS AND OUTLOOK

The results in this study provide valuable insights into the behavior and performance of the proposed approach under various

conditions. As demonstrated, the model accurately predicts the key parameters even in the presence of noise. This highlights the robustness and generalization ability of the approach.

To set the stage for future developments, we first provide an overview of the preliminary modifications to the initial results. In this context, R_s , which is previously considered constant under STC conditions, is included in the estimation.

In the following, we present the initial results by employing an adaptive loss weighting strategy. The introduction of the trainable scaling parameter α ensures improved convergence behavior, particularly in balancing the influence of data-driven and physics-based components during training.

The following analysis explores the impact of this data sparsity and discusses potential solutions to enhance the model's performance in these high-sensitivity regions.

A. Adaptive Loss Weighting

In the previous section, R_s is following STC assumptions. However, because R_s is highly sensitive to system degradation and fault conditions, excluding it from the estimation process limits the model's ability to extract meaningful diagnostic information. Therefore, the current framework treats R_s as an estimable parameter and includes it in the training process.

Another hand in the initial configuration, the weighting coefficients in the loss function, were selected manually through trial and error. To address this, the model uses an adaptive tuning mechanism by learning a trainable scaling parameter α . Instead of learning λ_1 and λ_2 directly, the following formulation is used [17]:

$$L_{\text{total}} = \frac{1}{2}e^{-\alpha}L_{\text{physics}} + \frac{1}{2}e^{\alpha}L_{\text{data}} + \eta\alpha^2 \quad (17)$$

where

- 1) α is a trainable parameter;
- 2) $e^{-\alpha}$ and e^{α} control the weights of the physics and data losses in log-space;
- 3) The regularization term $\eta\alpha^2$ prevents α from diverging.

This approach allows the model to balance the influence of physical constraints and data during training in a dynamic way.

Given that the transient parts of the signal typically contain high-frequency components and rapid variations, the model applies upsampling in those regions to improve the accuracy of parameters such as C_{j0} , which are particularly sensitive to transient behavior. By increasing the resolution in these regions, the model captures more detailed information about the system's dynamic response. The effect of this modification appears in the improved convergence of C_{j0} and its increased robustness to noise in the final estimation.

The model assigns random initial values to all parameters and trains using 150 data points taken from the transient region of the current response. The value of η is set to 10^{-4} during the training process.

The output current appears in Fig. 12, which shows that the response predicted by the PINN closely matches the true output throughout the transient region.

The network structure for parameter estimation follows the configuration presented in Table IV.

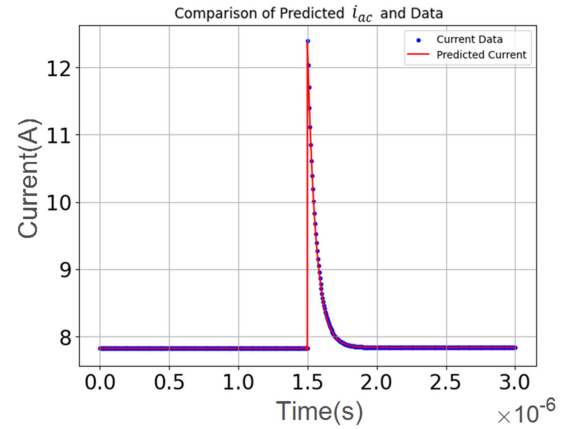


Fig. 12. Comparison between predicted current and observed data. The plot shows the true current measurements (blue dots) and the model-predicted current (red line).

TABLE IV
VALUE RANGES USED FOR EACH PARAMETER DURING TRAINING

Parameter	Range
G	[100 W/m ² , 2500 W/m ²]
T	[0 K, 400 K]
R_s	[0.1Ω, 0.35Ω]
C	[124.8 × 10 ⁻⁹ F, 374.4 × 10 ⁻⁹ F]

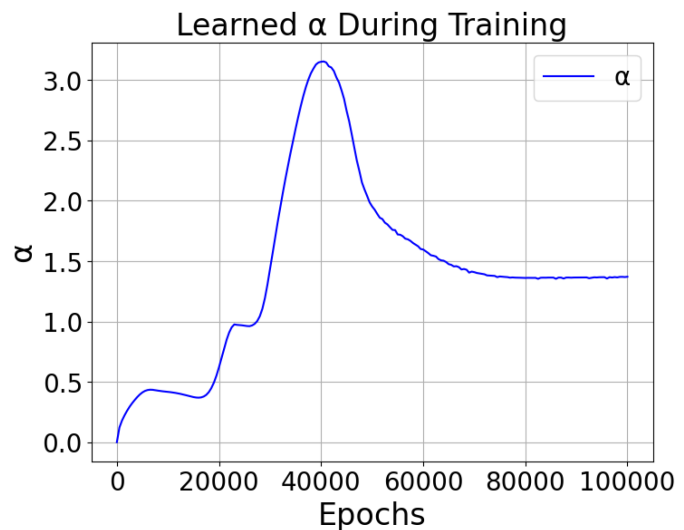


Fig. 13. Evolution of α during training.

Fig. 13 shows the convergence behavior of the adaptive weight parameter α .

The convergence of α to a positive value suggests that, while the model incorporates both data and physical constraints, the data component maintains a slightly stronger influence. This adaptive weighting strategy enables the model to dynamically adjust its focus throughout training, depending on which source of information provides more effective guidance, and ultimately leads to stable and reliable convergence.

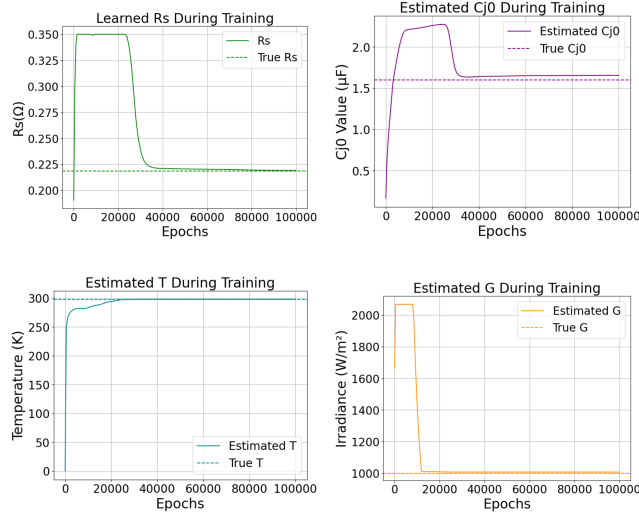


Fig. 14. Evolution of parameters during training: R_s , C_{j0} , T , and G .

Fig. 14 illustrates the convergence of the estimated parameters. As shown, the use of adaptive weighting through the dynamic adjustment of α improves parameter estimation performance and ensures more stable convergence behavior throughout training.

Moreover, this work investigates the behavior of the adaptive weighting factor λ (represented as α in the loss function), especially in relation to varying levels of input noise. It examines how noise impacts λ and explores strategies to enhance its robustness, aiming to achieve more stable and generalizable training in practical scenarios with imperfect data.

B. Sensitivity of R_s Estimation to Peak Data Loss

Accurate estimation of R_s heavily relies on the model's ability to capture sharp transitions in the current waveform, particularly during transient and peak regions. These segments often contain high-frequency components that reflect dynamic changes in the system. However, due to limited temporal resolution, the model frequently undersamples these peak regions, which leads to partial loss of informative features.

This limitation in data directly impacts the estimation of R_s , as the available information is insufficient to accurately capture the parameter's transient behavior (see Fig. 15).

Future work will focus on addressing the effects of missing or unreliable data, particularly in peak regions where measurement gaps or noise can significantly influence the estimation of sensitive parameters such as R_s . By incorporating physical knowledge into the loss function, the model is able to partially compensate for the missing information in the pick region.

The model is based on the single-diode representation of crystalline silicon photovoltaic module, capturing their physical and dynamic behavior. Although the electrical characteristics and parameter ranges may vary between module types such as CIGS [21], and CdTe [22], the underlying PINN framework is flexible and can be adapted accordingly. Also, the PINN approach shows high accuracy in estimating physical

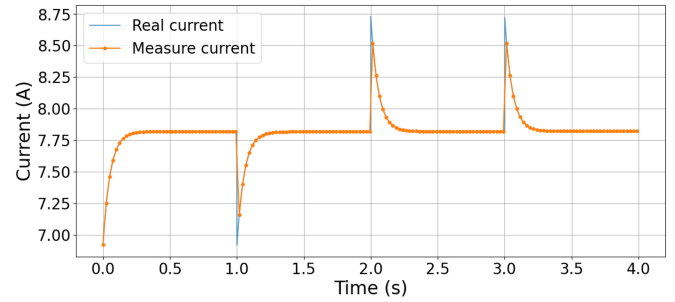


Fig. 15. Comparison of the real current and the measured current over time. The discrepancies between the two curves may arise in real-world scenarios due to factors such as measurement noise, sensor delays, limited sampling rates, or filtering applied during data acquisition. The measured waveform fails to accurately capture the sharp peak, potentially leading to significant information loss in transient regions that are essential for reliable estimation of R_s .

parameters, it does not consider computational latency or practical feasibility for real-time deployment. To address this, future work will explore integrating the PINN framework with time series architectures to better capture temporal dependencies while reducing inference time.

IX. CONCLUSION

In this study, to address the challenge of weak convergence in highly nonlinear parameters, a novel two-level layered framework based on PINNs is proposed. In this structure, two-level layered PINN has been designed. The first layer of network is used to estimate standard parameters such as R_s , R_{sh} , and I_{ph} with help estimation of T and G . The second layer of network, with a more complex architecture, is dedicated specifically to estimating C_{j0} , a parameter whose behavior is strongly nonlinear due to its dynamic dependence on both current and voltage. At the current stage, the proposed methodology has been evaluated using simulated time-domain waveforms, which allowed for flexible adjustment of the number of time samples and facilitated proper configuration of the PINN parameters. This study uses simulated dataset for having a full control of the input data to evaluate and quantify the effects of noise, under sampling, sampling that is not synchronized with the voltage change imposed by MPPT. The application of the proposed methodology to experimental waveforms is currently in progress, in order to assess its performance and reliability under realistic operating conditions. Future work will also focus on limitation data and automating the network weighting process in order to enhance adaptability and reduce reliance on manual calibration.

REFERENCES

- [1] M. D. Riso, I. Matacena, S. Daliento, and P. Guerriero, "Impedance spectroscopy as on-field monitoring technique for PV modules," in *Proc. 19th Conf. Ph.D. Res. Microelectron. Electron.*, Larnaca, Cyprus, 2024, pp. 1–4, doi: [10.1109/PRIME61930.2024.10559699](https://doi.org/10.1109/PRIME61930.2024.10559699).
- [2] N. Femia, G. Petrone, G. Spagnuolo, and M. Vitelli, *Power Electronics and Control Techniques for Maximum Energy Harvesting in Photovoltaic Systems*. Boca Raton, FL, USA: CRC Press, 2017.
- [3] M. D. Riso, I. Matacena, P. Guerriero, S. Daliento, L. E. G. Marrero, and G. Petrone, "Dynamic modeling of Si-based photovoltaic modules using impedance spectroscopy technique," in *Proc. Int. Conf. Clean Elect. Power*, 2023, pp. 430–435, doi: [10.1109/ICCEP57914.2023.10247369](https://doi.org/10.1109/ICCEP57914.2023.10247369).

- [4] L. E. Garcia-Marrero, C. I. Pavon-Vargas, J. D. Bastidas-Rodriguez, E. Monmasson, and G. Petrone, "Self-adaptive single-diode model parameter identification under small mismatching conditions," *Renewable Energy*, vol. 245, 2025, Art. no. 122735, doi: [10.1016/j.renene.2023.122735](https://doi.org/10.1016/j.renene.2023.122735).
- [5] J. D. Bastidas-Rodriguez, G. Petrone, C. A. Ramos-Paja, and G. Spagnuolo, "A genetic algorithm for identifying the single diode model parameters of a photovoltaic panel," *Math. Comput. Simul.*, vol. 131, pp. 38–54, 2017, doi: [10.1016/j.matcom.2015.12.003](https://doi.org/10.1016/j.matcom.2015.12.003).
- [6] J. Montano, L. F. Grisales Noreña, A. Tobón, and D. Gonzalez Montoya, "Estimation of the parameters of the mathematical model of an equivalent diode of a photovoltaic panel using a continuous genetic algorithm," *IEEE Latin America Trans.*, vol. 20, no. 4, pp. 616–623, Apr. 2022, doi: [10.1109/TLA.2022.9759926](https://doi.org/10.1109/TLA.2022.9759926).
- [7] M. Raissi, P. Perdikaris, and G. E. Karniadakis, "Physics-informed neural networks: A deep learning framework for solving forward and inverse problems involving nonlinear partial differential equations," *J. Comput. Phys.*, vol. 378, pp. 686–707, 2019, doi: [10.1016/j.jcp.2018.10.045](https://doi.org/10.1016/j.jcp.2018.10.045).
- [8] J. Stiasny, G. S. Misyris, and S. Chatzivasileiadis, "Physics-informed neural networks for non-linear system identification for power system dynamics," in *Proc. IEEE Madrid PowerTech*, 2021, pp. 1–6, doi: [10.1109/Powertech46648.2021.9495063](https://doi.org/10.1109/Powertech46648.2021.9495063).
- [9] R. A. Guejia-Burbano and G. Petrone, "Partial shading detection on PV panels through on-line impedance spectroscopy," in *Proc. IEEE Int. Conf. Environ. Elect. Eng.; IEEE Ind. Commercial Power Syst. Europe*, ZUZL, 2021, pp. 1–6, doi: [10.1109/EEEIC/ICPSEurope51590.2021.9584621](https://doi.org/10.1109/EEEIC/ICPSEurope51590.2021.9584621).
- [10] M. Pilouagine, P. Sánchez-Friera, and G. Spagnuolo, "Comparative of IEC 60891 and other procedures for temperature and irradiance corrections to measured I–V characteristics of photovoltaic devices," *Energies*, vol. 17, no. 3, 2024, Art. no. 566.
- [11] I. Mora-Seró, G. García-Belmonte, P. P. Boix, M. A. Vázquez, and J. Bisquert, "Impedance spectroscopy characterisation of highly efficient silicon solar cells under different light illumination intensities," *Energy Environ. Sci.*, vol. 2, no. 7, pp. 678–686, Jul. 2009, doi: [10.1039/b812468j](https://doi.org/10.1039/b812468j).
- [12] R. Faranda and S. Leva, "Energy comparison of MPPT techniques for PV systems," *WSEAS Trans. Power Syst.*, vol. 3, no. 6, pp. 446–455, 2008.
- [13] E. Haghigat, M. Raissi, A. Moure, H. Gomez, and R. Juanes, "A physics-informed deep learning framework for inversion and surrogate modeling in solid mechanics," *Comput. Methods Appl. Mech. Eng.*, vol. 379, 2021, Art. no. 113741, doi: [10.1016/j.cma.2021.113741](https://doi.org/10.1016/j.cma.2021.113741).
- [14] X.-Y. Guo and S.-E. Fang, "Structural parameter identification using physics-informed neural networks," *Measurement*, vol. 220, 2023, Art. no. 113334, doi: [10.1016/j.measurement.2023.113334](https://doi.org/10.1016/j.measurement.2023.113334).
- [15] Z. Zou, X. Meng, and G. E. Karniadakis, "Correcting model misspecification in physics-informed neural networks (PINNs)," *J. Comput. Phys.*, vol. 505, 2024, Art. no. 112918, doi: [10.1016/j.jcp.2024.112918](https://doi.org/10.1016/j.jcp.2024.112918).
- [16] S. Zhao, Y. Peng, Y. Zhang, and H. Wang, "Parameter estimation of power electronic converters with physics-informed machine learning," *IEEE Trans. Power Electron.*, vol. 37, no. 10, pp. 11567–11578, Oct. 2022, doi: [10.1109/TPEL.2022.3176468](https://doi.org/10.1109/TPEL.2022.3176468).
- [17] A. Kendall, Y. Gal, and R. Cipolla, "Multi-task learning using uncertainty to weigh losses for scene geometry and semantics," in *Proc. IEEE Conf. Comput. Vis. Pattern Recognit.*, Salt Lake City, UT, USA, 2018, pp. 7482–7491.
- [18] Z. Huang and Y. Wang, "Applications of physics-informed neural networks in power systems—A review," *IEEE Trans. Power Syst.*, vol. 38, no. 1, pp. 572–588, Jan. 2023, doi: [10.1109/TPWRS.2022.3206813](https://doi.org/10.1109/TPWRS.2022.3206813).
- [19] W. Wang and N. Yu, "Estimate three-phase distribution line parameters with physics-informed graphical learning method," *IEEE Trans. Power Syst.*, vol. 37, no. 5, pp. 3577–3588, Sep. 2022, doi: [10.1109/TPWRS.2021.3134952](https://doi.org/10.1109/TPWRS.2021.3134952).
- [20] W. Wang and N. Yu, "Physics-informed graph neural network for power systems state estimation with limited labeled data," *IEEE Trans. Power Syst.*, vol. 38, no. 1, pp. 783–794, Jan. 2023, doi: [10.1109/TPWRS.2022.3186509](https://doi.org/10.1109/TPWRS.2022.3186509).
- [21] F. Kessler and D. Rudmann, "Technological aspects of flexible CIGS solar cells and modules," *Sol. Energy*, vol. 77, no. 6, pp. 685–695, 2004.
- [22] I. E. Tinedert, F. Pezzimenti, M. L. Megherbi, and A. Saadoune, "Design and simulation of a high efficiency CDS/CDTE solar cell," *Optik*, vol. 208, 2020, Art. no. 164112.